Available online at www.sciencedirect.com
ScienceDirect
International Journal of Multiphase Flow 33 (2007) 809–821
International Journal of Multiphase Flow
www.elsevier.com/locate/ijmulflow

Experimental investigation of post-dryout heat transfer in annulus with spacers

Henryk Anglart *, Per Persson

Nuclear Reactor Technology, School of Engineering Sciences, Royal Institute of Technology, SE-106 91 Stockholm, Sweden

Received 3 November 2005; received in revised form 18 February 2007

Abstract

Experimental investigations of post-dryout heat transfer in 10×22.1 annulus test section with spacers were carried out in the high-pressure two-phase flow loop at the Royal Institute of Technology (KTH). The test section was manufactured of Inconel 600 to withstand high temperatures. Several thermocouples were installed on tube and rod surfaces to measure the local wall temperature. Measurements were performed for mass flow rate in range from 500 to 2000 kg m^{-2} s^{-1}, with inlet subcooling equal to 10 and 40 K, heat flux in a range from 480 to 1380 kW m^{-2} and for the system pressure of 7 MPa. Uniform axial power distributions were applied on rod and tube walls. Using different distributions of heat flux between walls, post-dryout was achieved either on the inner or on the outer wall. The experimental results indicate a very strong influence of spacers on post-dryout heat transfer. For low mass flow rates the wall superheat was significantly reduced downstream of spacers, even though the whole distance between spacers was still under post-dryout conditions when heat flux was high enough. At high mass flow rates and under investigated range of heat flux the dryout patches were effectively quenched downstream of spacers.

Keywords: Heat transfer; Post-dryout; Spacer influence

1. Introduction

Understanding of the post-dryout heat-transfer mechanism is very important for evaluation of safety features of Boiling Water Reactors (BWR). This type of heat-transfer regime is not allowed under normal operating conditions in BWRs, however, it may appear in some off-normal (steady-state or transient) situations. In such cases it is essential to be able to predict the maximum clad temperature as well as time history of the temperature distribution, since they determine the risk of the loss of integrity of the cladding. Therefore, a great amount of research has been devoted to study the post-dryout heat transfer, including both the experimental and the analytical work. An extensive compilation of some of these results can be found in Hewitt et al. (1993).

* Corresponding author. Tel.: +46 (0) 8 5537 8887; fax: +46 (0) 8 5537 8601.
E-mail address: henryk@kth.se (H. Anglart).

0301-9322/$ - see front matter © 2007 Elsevier Ltd. All rights reserved.
doi:10.1016/j.ijmultiphaseflow.2007.02.006

Early investigations of post-dryout were performed in tubes in which the influence of such parameters as mass flow rate and pressure was studied. Bennett et al. (1966), Wurtz (1978) and Becker et al. (1983) measured wall temperatures in uniformly heated tubes under post-dryout conditions for a wide range of pressure and mass flux. Tubes with non-uniform heating were used by Bennett et al. (1967) and Becker et al. (1992) to investigate the influence of axial power distributions on post-dryout heat transfer.

One of the important factors influencing post-dryout heat transfer is the presence of spacers in a heated channel. This influence has been studied both experimentally (e.g. Yao et al., 1982; Yoder et al., 1983) and analytically (e.g. Chiou et al., 1982; Sergeev, 2005). In the present study the effect of spacers has been investigated in an annulus with both tube and rod wall heated and using a modern BWR spacer design. The purpose of the study is to provide experimental data needed for validation of post-dryout heat-transfer models and, in particular, to study the effect of spacers on post-dryout heat transfer.

2. Experimental setup

The experiments were carried out in a high-pressure two-phase flow loop at the Royal Institute of Technology (KTH), Stockholm, Sweden. The schematic of the loop is shown in Fig. 1. It consists of one closed water circuit with maximum pressure of 25 MPa in which all parts in contact with water are made of stainless steel. Test sections with heated length up to 7300 mm can be studied, using direct current generator as the power supply. The maximum available current is 6 kA, with voltage ranging from 0 to 140 V. The inlet water temperature in the test section is adjusted in the 150-kW preheater. The main circulation pump has the maximum capacity of 1 kg s^{-1} and pressure head of 1 MPa. The major portion of this pressure head is used in the loop between the pump and the test-section inlet, thus providing sufficient throttling for stable operation of the loop.

The flow-meter system consists of four 1 m long tubes of 3.80, 6.29, 8.75 and 13.20 mm inner diameter. The flow rate measurements were performed through measurement of pressure drop over one of these tubes with a Barton cell. The accuracy of this flow meter system is estimated to be better than 1% in the whole range of applications (Becker and Hernborg, 1961).

The static pressure of the loop was measured with Barton cells connected to pressure taps, which were located just below and above the test section. The water temperature was measured at three locations: before the flow meter as well as below and after the test section.

The supplied power was obtained through measurement of the current through and the voltage over the test section. The voltage was measured with a precision voltometer of 0.25% rated accuracy, and the current was obtained by measuring the voltage over a calibrated shunt. In order to check the accuracy of the instrumen-

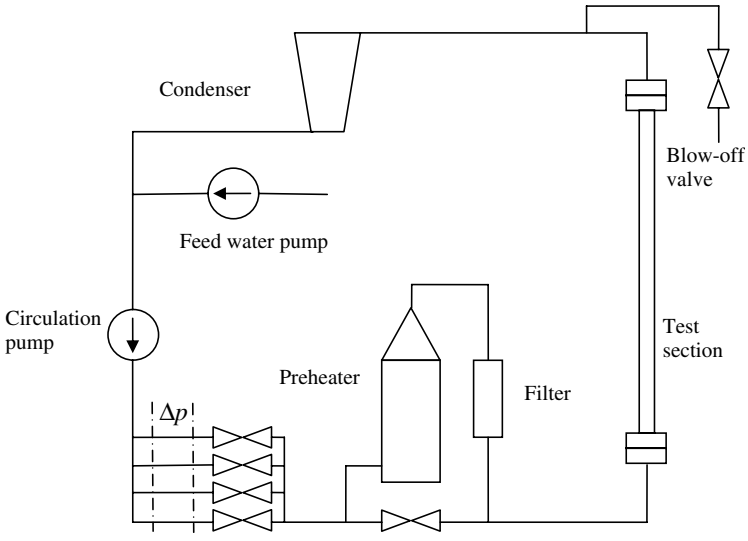

Fig. 1. Schematic of the experimental facility.

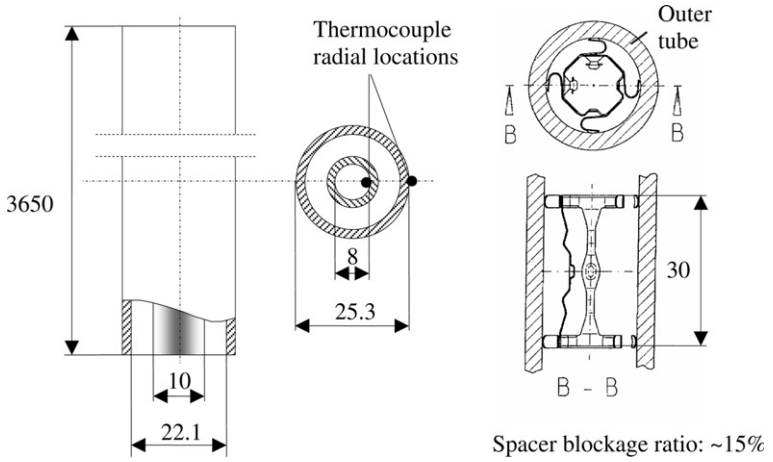

Fig. 2. Test-section details (all dimensions in mm).

tation, heat balance measurements for single-phase flow were taken. In general, the error in the heat balance was less than 1%.

Details of the test section are shown in Fig. 2. The test section consisted of 22.1×10 mm annulus, in which the inner rod (8×10 mm) and the outer tube (22.1×25.3 mm) were kept equidistant along the heated length using seven spacers. The heated length of the test section was equal to 3650 mm.

The axial locations of spacers and thermocouples are shown in Fig. 3. Fig. 3a shows distances of the lower (upstream) edge of spacers from the beginning of the heated length of the test section. The four uppermost spacers are 379 mm apart, whereas the distance between the remaining spacers is approximately equal to 560 mm. Fig. 3b and c shows the axial locations of thermocouples on rod and tube walls. The thermocouple locations were different for cases when post-dryout heat transfer was expected to occur on the rod surface (Fig. 3b) and on the tube surface (Fig. 3c). In the latter case the number of thermocouples on the tube wall was increased to 14, whereas the thermocouples on the rod surface were moved towards the exit of the test section.

The performance of thermocouples was tested by means of single-phase flow experiments in which the wall temperatures were measured and compared with predictions by the Dittus–Boelter correlation. The measurements were carried out in the annulus for mass flux equal to 500, 1000, 1500 and 2000 kg m^{-2} s^{-1}. Excluding points just downstream of spacers, where local heat-transfer enhancement was observed, the

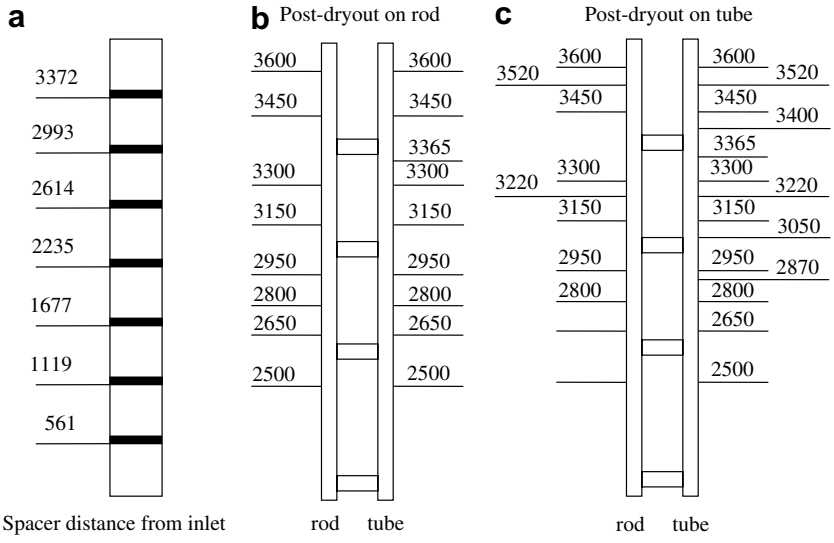

Fig. 3. Axial locations of spacers and thermocouples measured from the beginning of heated length (all dimensions in mm).

measured and calculated temperatures agreed with each other, with an estimated standard deviation smaller than 2 K.

3. Experimental matrix

The following operating conditions were used in experiments:

Pressure: 7 MPa
Inlet subcooling: 10 and 40 K
Mass flux: 500, 750, 1000, 1250, 1500, 1750 and 2000 kg m^{-2} s^{-1}
Heat flux: from 480 to 1380 kW m^{-2}

In all runs two-sided heating was applied. Runs 1–47 were designed in such a way that dryout and post-dryout occurred on the inner (rod) surface only. For that purpose the applied heat flux to both inner and outer walls was approximately equal to each other. Runs 48–65 were designed to obtain post-dryout conditions on the outer surface only. This required approximately 50% higher heat flux applied to that wall compared to the inner wall. The detailed working conditions for all experimental runs are shown in Table 1. The notation used in Table 1 is as follows: p – pressure at the test-section exit, ΔT_{sub} – inlet subcooling, G – mass flux, q''_i – heat flux at the inner wall, q''_o – heat flux at the outer wall.

Table 1
Working conditions for experimental runs

Run #	p (MPa)	ΔT_{sub} (K)	G (kg/(m^2 s))	q''_i (kW/m^2)	q''_o (kW/m^2)	Run #	p (MPa)	ΔT_{sub} (K)	G (kg/(m^2 s))	q''_i (kW/m^2)	q''_o (kW/m^2)
1	7.00	10.4	507	484.0	494.1	34	6.98	40.0	753	766.9	797.9
2	6.98	10.2	507	488.3	505.6	35	6.98	40.1	999	872.6	873.3
3	6.98	10.2	505	517.4	525.5	36	7.00	40.3	1006	886.6	907.8
4	6.96	9.8	507	543.5	554.7	37	7.00	40.3	1006	908.1	921.5
5	7.00	9.7	754	630.7	647.1	38	7.00	40.3	1004	935.9	953.4
6	7.00	10.3	753	651.4	671.8	39	7.00	40.3	1255	962.3	972.5
7	6.98	10.1	751	681.4	682.0	40	6.86	39.5	1252	985.3	999.3
8	6.98	10.0	750	693.8	712.6	41	7.00	40.3	1252	1019.9	1050.0
9	6.98	10.0	1006	748.7	785.2	42	6.98	40.1	1248	1068.3	1083.9
10	7.00	10.2	1003	767.5	798.6	43	6.98	40.1	1249	1101.0	1120.3
11	6.98	10.0	998	790.3	814.5	44	6.98	40.0	1506	1074.0	1088.3
12	7.00	10.2	1001	834.0	846.0	45	7.00	40.3	1506	1095.8	1103.3
13	7.03	10.4	1251	879.6	889.3	46	6.98	40.0	1498	1112.7	1132.0
14	7.00	10.2	1252	910.5	933.8	47	6.98	39.4	1514	1157.2	1174.6
15	6.98	10.0	1252	938.9	965.9	48	6.98	9.9	509	443.8	693.2
16	6.98	9.8	1506	994.0	1019.0	49	6.97	10.0	756	560.6	867.6
17	6.98	9.7	1504	1021.1	1050.0	50	7.00	10.0	754	569.9	885.1
18	7.00	10.6	1504	1044.3	1066.4	51	7.01	10.4	1000	626.4	983.1
19	6.96	10.1	1502	1071.5	1087.4	52	6.98	9.7	998	646.9	1016.8
20	7.00	9.9	1762	1050.0	1084.0	53	6.99	9.7	998	664.5	1033.6
21	7.00	9.9	1749	1104.9	1124.8	54	6.97	10.0	1255	710.3	1106.1
22	6.98	10.3	1756	1132.2	1156.4	55	6.96	9.7	1246	716.7	1128.2
23	6.98	10.3	1751	1156.5	1173.7	56	6.98	10.1	1258	733.3	1141.9
24	6.98	9.6	2000	1127.6	1140.9	57	6.98	10.2	1255	734.5	1144.4
25	6.98	10.2	1999	1156.5	1174.6	58	7.00	9.7	1500	747.3	1192.3
26	6.98	39.5	503	538.5	549.7	59	6.96	9.7	1497	754.5	1206.0
27	6.98	40.1	505	542.1	553.4	60	7.01	10.8	1505	757.9	1211.1
28	7.00	40.3	503	546.7	566.2	61	7.03	9.9	1748	791.4	1247.9
29	7.03	40.6	503	567.9	591.3	62	6.95	9.6	1749	816.9	1287.7
30	6.98	40.1	503	589.4	607.6	63	7.01	10.1	2000	842.7	1329.7
31	7.00	40.3	750	714.4	727.6	64	7.01	9.5	2002	859.7	1363.2
32	6.98	40.1	752	719.7	742.9	65	6.96	10.4	2007	866.9	1368.1
33	7.00	40.3	753	758.8	770.0						

4. Experimental results

For all cases shown in Table 1, wall temperatures were measured at locations indicated in Figs. 2 and 3. Tables 2 and 3 contain the measured rod and tube wall temperatures. It should be noted that values given in tables are thermocouple readings and thus correspond to rod inner surface and tube outer surface temperatures, in accordance with radial thermocouple locations shown in Fig. 2.

Table 2
Measured wall temperature (°C) on rod inner surface at various locations from the inlet

Run #	Distance from inlet (mm)							
	2500	2650	2800	2950	3150	3300	3450	3600
1	305.5	305.9	306.2	301.7	302.0	301.6	301.6	342.5
2	306.1	306.5	306.8	302.3	302.0	301.6	302.2	465.7
3	306.6	307.0	307.3	302.9	302.6	360.1	349.6	543.1
4	307.9	308.3	308.6	307.7	391.9	532.9	443.5	563.8
5	311.4	311.8	312.1	306.5	306.8	305.8	306.4	361.9
6	312.0	312.4	312.7	306.5	306.8	307.6	306.4	500.2
7	312.6	313.0	313.3	307.7	308.0	422.1	307.6	554.7
8	313.3	313.7	314.0	317.2	308.6	543.3	313.6	577.1
9	316.2	316.6	316.3	310.2	310.4	309.4	309.4	333.4
10	316.2	316.6	316.9	311.3	310.4	311.2	309.4	435.4
11	316.8	317.8	317.5	313.7	311.6	437.2	310.6	449.8
12	318.6	319.0	319.3	529.7	312.2	557.1	312.4	534.1
13	320.3	320.1	321.0	314.3	313.9	313.5	312.4	332.8
14	321.5	321.9	322.2	376.1	314.5	366.7	313.6	406.0
15	322.1	322.5	323.3	554.9	315.1	422.2	314.1	414.7
16	325.2	325.0	325.3	318.5	317.0	317.2	316.1	337.6
17	326.4	326.3	326.5	360.7	317.7	331.4	317.3	393.0
18	326.3	326.7	327.0	445.6	318.2	386.0	317.3	400.4
19	327.6	328.0	328.3	593.6	318.9	436.3	318.5	458.1
20	326.4	326.8	327.1	319.2	318.9	318.5	317.9	335.4
21	328.8	329.2	329.5	361.2	320.1	344.2	319.1	388.3
22	329.9	329.8	330.0	491.0	320.6	349.5	319.7	443.7
23	330.5	330.9	331.2	590.7	321.2	408.1	320.9	526.4
24	329.4	328.7	329.6	321.6	320.7	320.9	319.8	345.4
25	330.0	329.8	330.7	322.8	321.9	321.5	320.4	376.2
26	307.2	307.6	307.9	303.5	303.1	302.7	302.7	316.7
27	307.8	307.6	307.9	303.5	303.1	302.7	302.7	390.7
28	307.8	308.2	308.5	303.5	303.7	302.7	306.3	516.1
29	308.9	308.8	309.0	304.0	303.7	366.4	436.4	560.8
30	310.1	309.9	310.2	304.6	322.5	534.5	483.5	578.6
31	314.3	314.7	314.4	308.8	308.5	308.7	305.8	325.0
32	314.8	314.6	314.9	308.7	308.4	308.6	306.3	433.5
33	315.4	315.8	316.1	309.9	309.6	330.9	343.7	539.6
34	316.7	316.5	316.8	310.6	310.3	551.2	355.5	546.6
35	320.1	319.9	320.2	313.4	313.1	312.7	–	320.3
36	320.7	320.5	321.4	314.0	313.7	315.6	–	404.1
37	321.8	321.7	321.9	314.6	314.3	357.1	–	501.2
38	322.4	322.2	323.1	315.2	314.9	517.3	318.6	539.6
39	323.6	323.4	323.7	315.8	316.0	315.6	313.3	325.5
40	324.2	324.0	324.3	316.4	316.0	315.6	313.3	382.6
41	325.4	325.2	326.0	318.1	317.2	329.1	313.9	485.2
42	327.1	326.9	327.8	319.3	319.0	443.3	317.4	553.4
43	328.3	328.1	329.0	320.5	320.1	564.3	329.7	598.7
44	327.8	327.0	327.9	319.4	319.1	318.7	318.1	340.2
45	327.8	327.6	328.5	320.0	319.6	319.3	318.7	383.3
46	328.8	329.6	320.6	320.2	319.8	319.3	473.8	473.8
47	329.9	330.8	321.7	321.4	360.1	316.9	436.4	436.4

Table 3
Measured wall temperature (°C) on tube outer surface at various locations from the inlet

Run #	Distance from inlet (mm)													
	2500	2650	2800	2870	2950	3050	3150	3220	3300	3365	3400	3450	3520	3600
48	322.2	321.0	321.9	319.3	321.0	318.3	320.4	320.4	320.8	318.5	315.3	318.3	377.8	433.6
49	331.0	329.8	330.5	328.2	329.9	326.7	327.0	323.9	324.2	326.9	323.2	324.7	356.2	391.0
50	332.0	330.5	331.1	329.0	330.5	327.5	327.7	324.7	325.3	327.6	324.7	325.3	401.5	511.7
51	336.5	334.7	335.9	333.5	334.8	331.5	331.8	329.0	329.5	332.0	328.9	329.9	331.2	364.5
52	338.2	336.0	337.1	334.8	336.3	332.8	333.1	330.4	330.7	338.9	335.4	332.5	336.6	498.2
53	338.9	336.9	337.9	335.4	337.1	333.4	334.1	330.7	337.1	358.1	358.1	334.7	351.7	–
54	342.0	339.7	341.1	338.5	340.1	336.3	337.2	333.8	334.3	337.2	333.7	334.3	335.5	369.8
55	343.3	340.7	342.4	339.8	341.3	337.5	338.3	335.2	335.5	507.3	362.0	336.4	336.6	346.9
56	343.9	341.5	342.9	340.2	341.9	338.0	339.0	335.7	337.2	548.8	373.1	337.3	337.2	344.8
57	344.2	341.9	343.2	340.7	342.4	338.6	339.3	336.4	340.7	568.5	393.5	339.6	338.4	346.5
58	346.1	343.5	344.9	342.6	344.1	339.8	340.8	337.9	338.1	391.3	338.5	338.5	339.1	338.5
59	346.6	344.3	345.5	343.1	344.5	340.8	341.4	338.5	339.0	572.2	361.8	339.2	340.1	352.5
60	347.0	344.4	345.8	343.3	345.0	341.0	342.0	338.7	339.7	524.6	373.5	339.7	340.3	347.9
61	349.1	346.5	348.0	345.6	347.3	343.3	344.0	341.0	341.3	365.4	348.8	341.5	342.6	346.1
62	350.3	347.8	349.4	346.8	348.6	344.5	345.2	342.4	345.1	561.0	385.8	344.5	343.9	351.4
63	352.3	349.8	351.1	349.2	350.3	346.4	347.4	344.5	344.5	363.1	346.8	344.7	345.9	349.2
64	353.9	351.0	352.7	350.3	352.0	348.0	348.8	346.2	346.3	450.5	385.8	347.3	347.5	352.5
65	353.9	350.8	352.7	350.2	351.7	348.0	348.7	346.2	346.3	588.5	378.3	347.5	347.5	353.3

5. Data analysis

The surface superheat, defined as a difference between the surface and the saturation temperatures, can be calculated from data in Tables 2 and 3 and from the temperature drop in heated walls. Table 4 shows the thermal conductivity of Inconel-600 used in calculations. Figs. 4–7, show the surface superheat as a function of the axial distance for various operating conditions.

As can be seen in Fig. 4, the initial dryout patch appears at the exit of the test section, when the heat flux on the inner wall is equal to 484 kW m^{-2}. Further increasing of the heat flux to 488.3 kW m^{-2} causes increase of the rod surface superheat by about 120 K, but the dryout patch is still limited to the region located downstream of the uppermost spacer. Only when heat flux on the inner wall exceeds 517 kW m^{-2} the dryout patch extends from a position upstream of the last spacer to the channel exit. It should be noted that the rod surface superheat is increasing while moving towards the channel exit, except for locations just downstream of a spacer, where local reduction of the wall temperature can be observed.

The influence of mass flux on post-dryout heat transfer can be seen in Figs. 4 and 5. Similarly as in channels without spacers, the wall superheat first increases and then decreases when mass flux in the channel is high. This can be observed in Fig. 5, where the maximum superheat of the rod surface appears just upstream of spacer number 6. It is interesting to see that spacers 6 and 7 are causing effective quenching of dryout patches in the investigated range of heat flux.

The influence of the inlet subcooling can be seen by comparing measurements shown in Figs. 5 and 6. Unlike in Fig. 5, the superheat of the rod wall keeps increasing when moving towards the channel exit, even though the dryout patch is effectively quenched downstream of the last spacer. The qualitative difference between Figs. 5 and 6 can be explained as follows. In both cases all parameters but inlet subcooling and heat flux are the same. Since the heat flux is uniformly distributed along the channel, both cases are equivalent with proper scaling. For channel with higher inlet subcooling and correspondingly higher heat flux, the total increase of quality between two neighboring spacers becomes higher. Further inspection of data reveals that

Table 4
Thermal conductivity of Inconel-600 (manufacturer's data)

Temperature (°C)	21	93	204	316	427	538	649
Conductivity (W m^{-1} K^{-1})	14.9	15.8	17.5	19.2	21.0	22.9	24.9

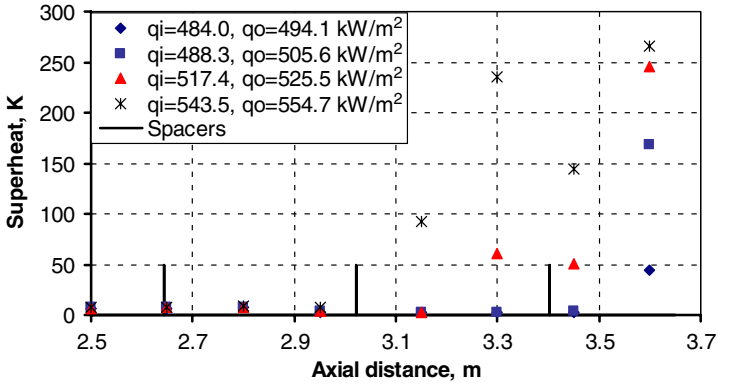

Fig. 4. Measured superheat of rod surface for runs 1–4. Mass flux $G = 500\ \mathrm{kg\,m^{-2}\,s^{-1}}$, inlet subcooling $\Delta T_{\mathrm{sub}} = 10\ \mathrm{K}$, pressure $p = 7\ \mathrm{MPa}$.

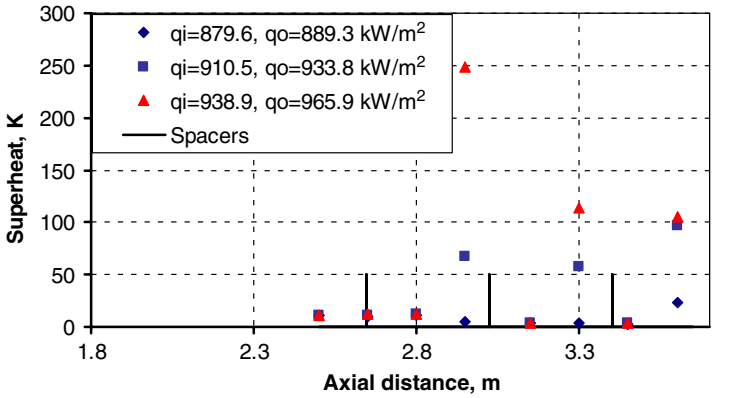

Fig. 5. Measured superheat of rod surface for runs 13–15. Mass flux $G = 1250\ \mathrm{kg\,m^{-2}\,s^{-1}}$, inlet subcooling $\Delta T_{\mathrm{sub}} = 10\ \mathrm{K}$, pressure $p = 7\ \mathrm{MPa}$.

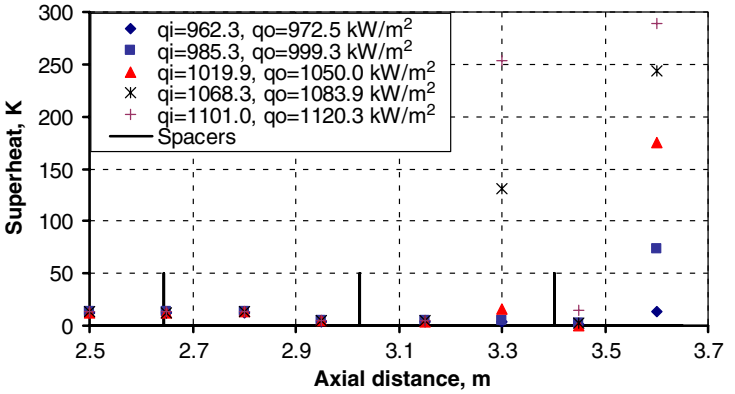

Fig. 6. Measured superheat of rod surface for runs 39–43. Mass flux $G = 1250\ \mathrm{kg\,m^{-2}\,s^{-1}}$, inlet subcooling $\Delta T_{\mathrm{sub}} = 40\ \mathrm{K}$, pressure $p = 7\ \mathrm{MPa}$.

the equilibrium quality at the post-dryout patches is also higher, as compared to cases with the lower inlet subcooling. As a result fewer water droplets are available in the gas core and thus cooling of the uncovered

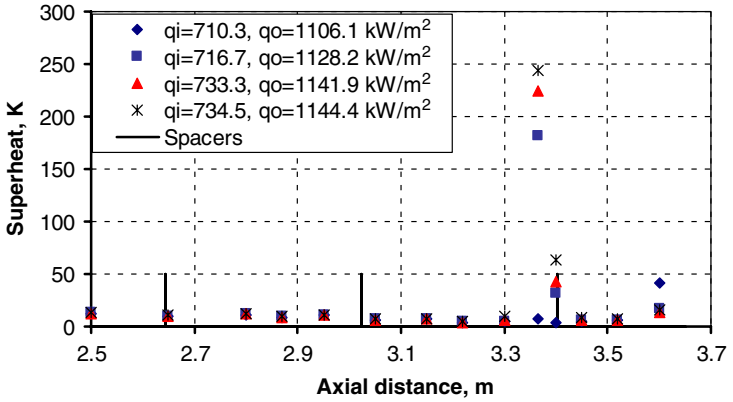

Fig. 7. Measured superheat of tube surface for runs 54–57. Mass flux $G = 1250\ \mathrm{kg\,m^{-2}\,s^{-1}}$, inlet subcooling $\Delta T_{\mathrm{sub}} = 10\ \mathrm{K}$, pressure $p = 7\ \mathrm{MPa}$.

surfaces is less effective. This phenomenon, combined with higher wall heat flux results in increasing wall superheat, as shown in Fig. 6.

Fig. 7 shows measured superheat of the tube wall for the same flow conditions as used in Fig. 5. As can be seen, dryout patch in Fig. 7 is limited to just upstream of the last spacer and then it is effectively quenched. This result, which is typical for all cases with dryout occurring on the tube surface, indicates that spacers are relatively more effective in quenching dryout patches on tubes compared with rods.

Figs. 8 and 9 show a comparison of the measured wall superheat in tube (Becker et al., 1983) and annulus versus the equilibrium quality. For relatively low Reynolds number ($\sim 8 \times 10^5$, based on vapour properties) the critical equilibrium quality in tube is slightly above 0.6, as can be seen in Fig. 8. For the same flow conditions, the critical equilibrium quality in annulus varies between 0.4 and 0.6 and in all cases is lower than the value observed in tube. The spread of the annulus data depends on the downstream distance to a spacer. The lowest critical quality in annulus can be observed for dryout on the inner surface, and slightly higher in cases when the inlet subcooling is equal to 40 K (data points marked with triangles in Fig. 8). For the outer surface the critical quality increases to ~0.55. When vapour-based Reynolds number is increased to $\sim 1.2 \times 10^6$, the critical quality in tube decreases to ~0.48, whereas the measured critical quality in annulus remains between ~0.4 and ~0.43, as shown in Fig. 9.

These points in Figs. 8 and 9 that clearly correspond to the post-dryout heat-transfer conditions are shown in Figs. 10 and 11 by plotting the Nusselt number against the equilibrium quality. The data points obtained in a tube are compared with predictions using the Groeneveld (1973) correlation, which is given as

$$Nu_{\mathrm{g}} = \frac{hD_{\mathrm{h}}}{\lambda_{\mathrm{g}}} = a\left[\left(\frac{GD_{\mathrm{h}}}{\mu_{\mathrm{g}}}\right)\left(x_{\mathrm{e}} + \frac{\rho_{\mathrm{g}}}{\rho_{\mathrm{f}}}(1 - x_{\mathrm{e}})\right)\right]^{b} Pr_{\mathrm{g,w}}^{c} Y^{d}, \tag{1}$$

where

$$Y = 1 - 0.1\left(\frac{\rho_{\mathrm{f}}}{\rho_{\mathrm{g}}} - 1\right)^{0.4}(1 - x_{\mathrm{e}})^{0.4}. \tag{2}$$

Here D_{h} is the hydraulic diameter, x_{e} is the equilibrium quality, ρ_{f} is the liquid density at saturation and ρ_{g}, μ_{g} and λ_{g} are density, dynamic viscosity and thermal conductivity of the vapour phase at saturation, respectively. The vapour-phase Prandtl number, $Pr_{\mathrm{v,w}}$, appearing in Eq. (1) is evaluated at the wall temperature. The recommended values of coefficients a, b, c and d for tubes are as follows: $a = 0.00109$, $b = 0.989$, $c = 1.41$ and $d = -1.15$, and for annuli: $a = 0.0520$, $b = 0.688$, $c = 1.26$ and $d = -1.06$.

It can be observed that the Nusselt numbers obtained from the data measured in annulus significantly depart from both the Becker data and from the Groeneveld correlation. The spread in the annulus data

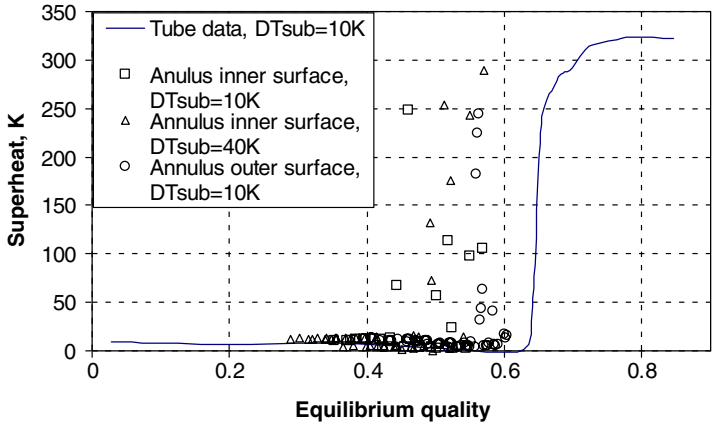

Fig. 8. Wall superheat in tube (Becker et al., 1983) and annulus (present measurements) as a function of equilibrium quality for pressure $p = 7$ MPa and vapour-based Reynolds number $\sim 8 \times 10^5$.

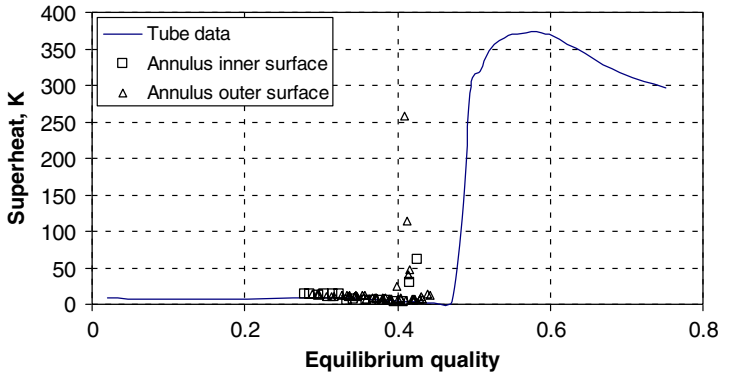

Fig. 9. Wall superheat in tube (Becker et al., 1983) and annulus (present measurements) as a function of equilibrium quality for pressure $p = 7$ MPa, inlet subcooling $\Delta T_{sub} = 10$ K and vapour-based Reynolds number $\sim 1.2 \times 10^6$.

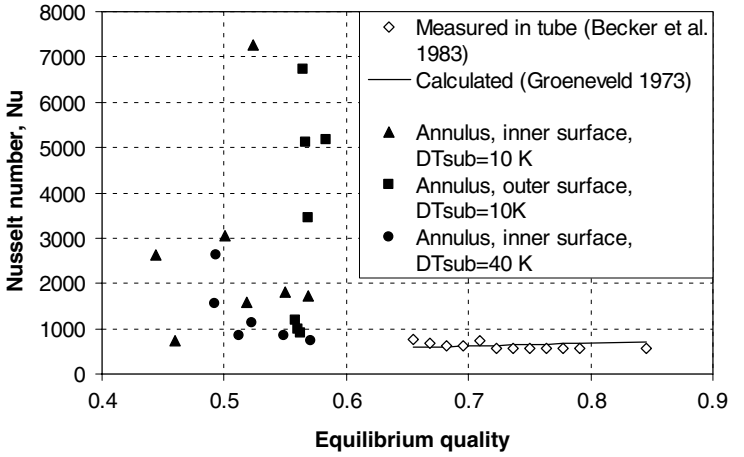

Fig. 10. Vapor-based Nusselt number as a function of equilibrium quality for $p = 7$ MPa and vapour-based Reynolds number $\sim 8 \times 10^5$.

can be attributed to the presence of spacers and to various distances between spacers and the locations where wall temperatures were measured.

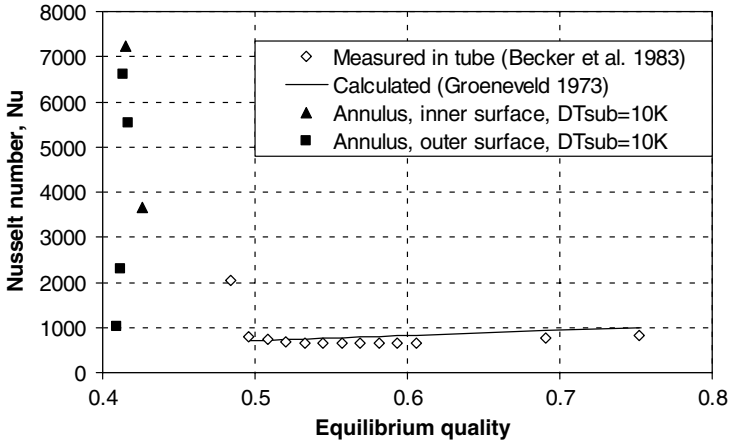

Fig. 11. Vapor-based Nusselt number as a function of equilibrium quality for $p = 7$ MPa and vapour-based Reynolds number $\sim 1.2 \times 10^6$.

Ideally, the effect of spacers should be investigated by comparing measurements performed in an annulus with and without spacers. Due to lack of the latter data, the Groeneveld correlation (Eqs. (1) and (2)) will be used to obtain the Nusselt number for post-dryout heat transfer in annuli without spacers.

The effect of straight spacers on heat transfer at single-phase flow was investigated by Yao et al. (1982). They proposed the following correlation to take into account the heat-transfer augmentation due to spacers:

$$\frac{Nu}{Nu_0} = 1 + 5.55 a_r^2 \cdot e^{-0.13\frac{z}{D_h}}, \tag{3}$$

where Nu is the Nusselt number in a channel with spacers, Nu_0 is the Nusselt number in a reference channel without spacers, a_r is the percent blockage of the channel flow area by the spacer, z is the axial distance downstream of the spacer and D_h is the channel hydraulic diameter. Since Eq. (3) is derived for single-phase flow, its application is limited to high quality dispersed flows. In addition, the correlation is valid for $Re > 10^4$ and $0.256 < a_r < 0.348$, and thus, it is not applicable for present spacers, which have a_r approximately equal to 0.15.

Groeneveld et al. (1999) proposed a correlation to cover a wider range of quality and also which is applicable for various types of spacers. They arrived at the following expression:

$$\frac{Nu}{Nu_0} = 1 + [0.47 + 4.81 \cdot x_e(1 - x_e)^{0.105}] \cdot K_{sp} \cdot e^{-0.13\frac{z}{D_h}}, \tag{4}$$

where x_e is the equilibrium quality and K_{sp} is the single-phase loss coefficient of the spacer. Correlation given by Eq. (4) can be used to calculate the heat-transfer augmentation factor, defined as $Nu/Nu_0 - 1$. Substituting $K_{sp} = 0.6$, which is a typical value of the loss coefficient for spacers used in present experiments and using equilibrium quality x_e equal to 0.4 and 0.6 it can be found that the maximum value of the factor is at $z = 0$ and is equal to 1.4 and 1.83, respectively.

The measured heat-transfer augmentation due to spacers, using the reference Nusselt number Nu_0 obtained from Eq. (1), is shown in Fig. 12. As can be seen the measured augmentation fraction is much higher than the fraction obtained from Eq. (4). Qualitatively Fig. 12 is not in agreement with Eqs. (3) and (4) either. While correlations predict the maximum augmentation fraction just downstream of the spacer, results which are shown in Fig. 12 exhibit the maximum at a certain distance downstream of the spacer, even though, in both cases the augmentation decays with increasing distance downstream of the spacer.

The main reason for discrepancies between measured data and correlations is that the post-dryout heat transfer in channels with spacers is never fully developed, provided that the distance between spacers is not very long, as in present experiments. In the developing region the wall superheat typically increases with a steep gradient until it reaches a maximum value. This behaviour can be observed for tube data shown in

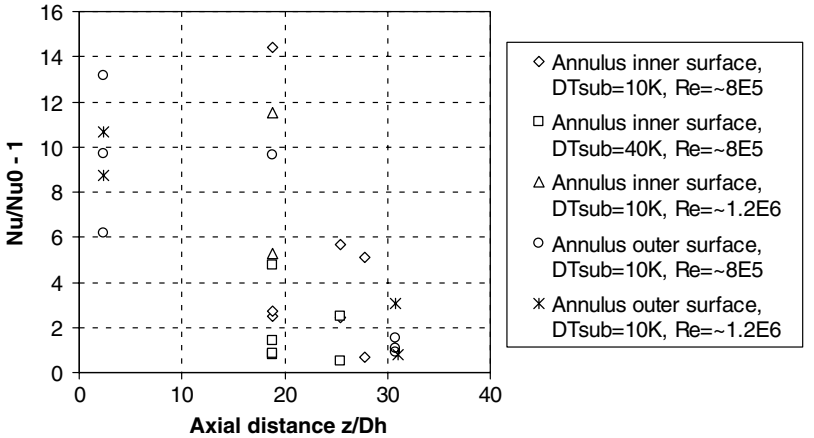

Fig. 12. Heat-transfer augmentation versus axial distance downstream of a spacer for post-dryout heat transfer in annulus with spacers.

Figs. 8 and 9. From the wall superheat data shown in Figs. 4–7 it is clear that the liquid film is partly, or even fully, restored downstream of spacers and the dryout patches only re-establish in the vicinity of the next spacer. This is particularly evident when inspecting data shown in Fig. 5.

Another important reason for observed discrepancies stems from the different heat-transfer augmentation mechanisms which are included in correlations given by Eqs. (3) and (4) and which in fact may play role. The main mechanism underlying correlations is the analogy between heat transfer and turbulence development downstream of a grid obstacle. It is well known, however, that spacers are causing an essential increase of liquid deposition to channel walls, both directly, by leading water from spacer surface to walls, and indirectly, by increasing drop deposition rates. These mechanisms are responsible for the restoration of the liquid film downstream of spacers observed in present experiments.

Figs. 13 and 14 show a comparison between the measured and the calculated from Eqs. (1), (2) and (4) effect of spacers on post-dryout heat transfer. The figures indicate that the discrepancy between the measured and the calculated Nusselt number decreases with increasing quality. This can be clearly seen in (Fig. 14a), which shows the Nusselt number ratio for low mass flow rate, when the quality in the post-dryout region is quite high. In particular, the experimental data are in good agreement with predictions when the quality is higher than 0.75. This is consistent with previous observation that the correlations are applicable for conditions when drop deposition rates are low, that is when quality is high. For low quality, however, Figs. 13 and 14 suggest that the effect of drop deposition on heat transfer is significantly under-predicted.

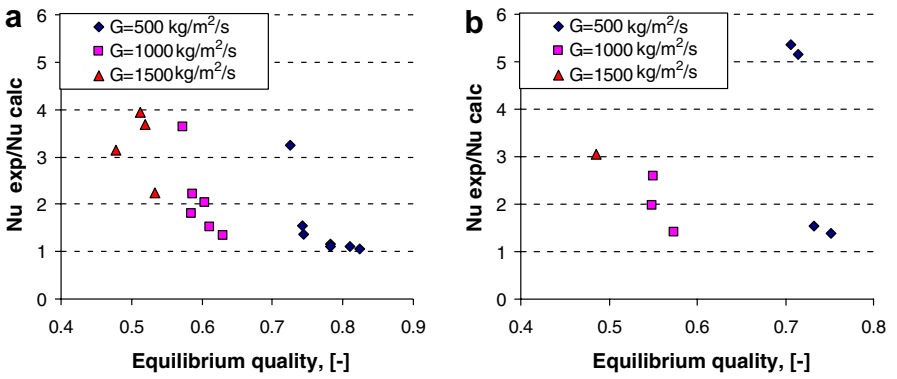

Fig. 13. Ratio of measured and calculated (Eqs. (1), (2) and (4)) Nusselt number on the inner wall surface as a function of equilibrium quality and mass flux for axial distance from the spacer equal to $z/D_h = 18.8$ (a) and for $z/D_h = 25.4$ (b).

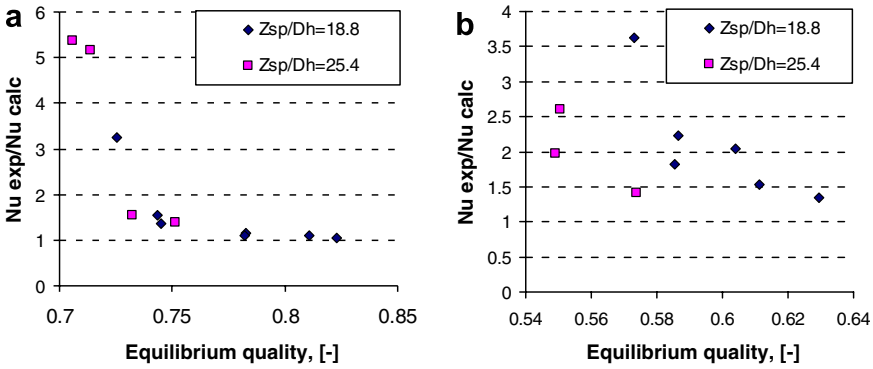

Fig. 14. Ratio of measured and calculated (Eqs. (1), (2) and (4)) Nusselt number on the inner wall surface as a function of equilibrium quality and distance from the spacer for mass flux $G = 500\ \mathrm{kg\,m^{-2}\,s^{-1}}$ (a) and $G = 1000\ \mathrm{kg\,m^{-2}\,s^{-1}}$ (b).

6. Conclusions

This paper presents experimental investigations of post-dryout heat transfer in an annulus with spacers. The wall superheat was measured at several axial positions on both rod and tube wall for a wide range of operating conditions. The main finding is that spacers have a very strong influence on post-dryout heat transfer, significantly reducing the wall superheat downstream of their location. For low mass flux a reduction of the wall superheat was observed, but for a sufficiently high heat flux, the whole distance between spacers was still under post-dryout heat-transfer conditions. For high mass flow rates and under investigated range of heat fluxes the dryout patches were effectively quenched downstream of spacers. Comparison of present results with selected correlations for heat-transfer augmentation due to spacers indicates that the effect of spacers can be significantly under-predicted. This is particularly true for low-quality post-dryout heat transfer, when drop deposition rates due to spacers are high and contribute to additional heat-transfer augmentation. Clearly more research, both theoretical and experimental, is needed to elucidate the mechanisms that govern the post-dryout heat transfer in channels with spacers.

Acknowledgements

The financial support provided by the Swedish Nuclear Inspectorate (SKI) is gratefully acknowledged. The authors are grateful to Mr. Stellan Hedberg for his assistance in performing the experiments.

References

Becker, K.M., Hernborg, G., 1961. Development and description of a novel method for accurate measurements of fluid flow rates. Report AE-RPL-102.

Becker, K.M., Ling, C.H., Hedberg, S., Strand, G., 1983. An experimental investigation of post-dryout heat tansfer. Report KTH-NEL-33, Royal Institute of Technology, Stockholm, Sweden.

Becker, K.M., Askeljung, P., Hedberg, S., Söderquist, B., Kahlbom, U., 1992. An experimental investigation of the influence of axial heat flux distributions on post dryout heat transfer for flow of water in vertical tubes. Report KTH-NEL-54, Royal Institute of Technology, Stockholm, Sweden.

Bennett, A.W., Hewitt, G.F., Kearsey, H.A., Keeys, R.F.K., Pulling, D.J., 1966. Studies of burnout in boiling heat transfer to water in round tubes with non-uniform heating. UKEA Report No. AERE-R 5076.

Bennett, A.W., Hewitt, G.F., Kearsey, H.A., Keeys, R.F.K., 1967. Heat transfer to steam–water mixtures flowing in uniformly heated tubes in which the critical heat flux has been exceeded. UKEA Report No. AERE-R 5373.

Chiou, J., Hochreiter, L.E., Utton, D.B., Young, M.Y., 1982. Spacer grid heat transfer during reflood. Joint NRC/ANS Meeting on Basic Thermal Hydraulic Mechanisms in LWR Analysis, NUREG-CP-0043.

Groeneveld, D.C., 1973. Post-dryout heat transfer et reactor operating conditions. Report AECL-4513.

Groeneveld, D.C., Leung, L.K.H., Zhang, J., Cheng S.C., Vasic, A., 1999. Effect of appendages on film-boiling heat transfer in tubes. In: Proceedings of the 9th International Topical Meeting on Nuclear Reactor Thermal-Hydraulics, San Francisco, USA.

Hewitt, G.F., Delhaye, J.M., Zuber, N. (Eds.), 1993. Post-dryout Heat Transfer. CRC Press, FL.

Sergeev, V., 2005. One dimensional model pf post-dryout heat transfer. In: Proceedings of the 11th International Topical Meeting on Nuclear Reactor Thermal-Hydraulics, Avignon, France.

Wurtz, J., 1978. An experimental and theoretical investigation of annular steam–water flow in tubes and annuli at 30–90 bar. RISØ Report No. 372.

Yao, S.C., Hochreiter, L.E., Leech, W.J., 1982. Heat transfer augmentation in rod bundles near grid spacers. J. Heat Transfer 104, 76–82.

Yoder Jr., G.L., Morris, D.G., Mullins, C.B., 1983. Dispersed-flow film boiling heat transfer data near spacer grids in a rod bundle. Nucl. Technol. 60, 303–314.